



Going Low in a World Going High: The Physiologic Use of Lower Frequency Electron Paramagnetic Resonance

Howard J. Halpern^{1,2} · Boris M. Epel^{1,2}

Received: 5 July 2020 / Revised: 20 August 2020 / Published online: 18 October 2020
© Springer-Verlag GmbH Austria, part of Springer Nature 2020

Abstract

Yakov Sergeevich Lebedev was a pioneer in high-frequency EPR, taking advantage of the separation of *g*-factor anisotropy effects from nuclear hyperfine splitting and the higher-frequency molecular motion sensitivity from higher-frequency measurements (Appl Magn Reson 7: 339–362, 1994). This article celebrates a second EPR subfield in which Prof. Lebedev pioneered, EPR imaging (Chem Phys Lett 99: 301–304, 1983). We celebrate the clinical enhancements that are suggested in this low-frequency work and imaging application to animal physiology at lower-than-standard EPR frequencies.

Abbreviations

EPR	Electron paramagnetic resonance
O ₂	Molecular oxygen
pO ₂	Partial pressure of dissolved molecular oxygen
MHz	Megahertz, units of 10 ⁶ Hz
WWII	World war two
RF	Radiofrequency
ρ	Charge density
J	Current density
σ	Material conductivity
E	Electric field intensity
B	Magnetic field induction
ω	Electric and magnetic field temporal angular frequency
ν	Electric and magnetic field temporal frequency
λ	Wavelength
k	Wave number = $2\pi/\lambda$
ϵ	Local material permittivity

✉ Howard J. Halpern
h-halpern@uchicago.edu

¹ Center for EPR Imaging in Vivo Physiology, University of Chicago, Chicago, USA

² Department of Radiation and Cellular Oncology, University of Chicago, Chicago, USA

μ	Local material permeability
ESE	Electron spin echo
SLR	Spin lattice relaxation
IRESE	Inversion recovery electron spin echo, a SLR based but echo detected measurement used in pO ₂ imaging
OX071	Also known as OX063d ₂₄ , the spin probe capable of quantitative pO ₂ imaging
<i>R1e</i>	Longitudinal electron relaxation rate
<i>R2e</i>	Transverse electron relaxation rate
<i>T1e</i>	1/ <i>R1e</i> Longitudinal electron relaxation time for signal reduction by 1/ <i>e</i>
<i>T2e</i>	1/ <i>R2e</i> Transverse electron relaxation time for signal reduction by 1/ <i>e</i>
CW	Continuous wave (measurement technique)
τ	Delay time between (1) the 90° pulse rotating magnetization initially oriented in the direction of the tmain magnetic field to a direction transverse to that direction, allowing regions of higher or lower magnetic field to develop larger or smaller phase delays and (2) the 180° pulse rotating the magnetization about the main magnetic field direction to correct for the local magnetic field inhomogeneities leaving only information from intrinsic transverse relaxation processes.
<i>T</i>	Delay time between (1) the 180° pulse rotating magnetization initially oriented in the direction of the tmain magnetic field to the opposite direction and (2) the 90° pulse rotating magnetization to a direction transverse to that direction, the beginning of a fixed τ electron spin echo magnetization readout
mT	Millitesla
mT/m	Millitesla/meter measure of magnetic field gradient strength
TCD	Tumor control dose
TCDn	Tumor control fraction n at a particular dose
Gy	Radiation dose in Joules of energy deposited per Kg material
FSa	A mouse fibrosarcoma tumor type grown in the progeny of the specific mouse type referred to as C3H that originally developed the fibrosarcoma in response to irritation from repeated application of methylcholanthrine dye
MCa4	A mammary carcinoma that developed spontaneously in the same mouse type as the FSa fibrosarcoma and grown in the C3H mouse type progeny.
RTOG	Radiation Therapy Oncology Group, a US national cooperative group organized for the purpose of conducting radiation therapy research and clinical investigations.
XRAD225Cx	Precision x-ray small animal x-ray radiator and computed tomography machine, North Branford, CT

1 Introduction

1.1 Short History of Low-Frequency EPR

Yevgeny Zavoisky's observation of resonant absorption of electromagnetic energy was the first observation of spin magnetic resonance in liquid copper chloride solutions although spin magnetic resonance had been long predicted. The resonance frequency was 133 MHz in a 47.6 Gauss electromagnet [1]. As expected, the EPR was born at low field. The development of radar during the preparation for WWII stimulated the development of higher-frequency and higher-power RF/microwave devices eventually including the magnetron, the klystron and other devices propelling the increase of spectral information available from those devices. In this tribute to Yacov Lebedev, who pioneered or at least was among the pioneers of EPR at thousand times the frequency used by Zavoisky [2], we think it useful to recognize that important biologically relevant and possibly medically relevant information can be obtained through another of Professor Lebedev's pioneering work, that in EPR imaging [3]. In lossy animal systems, this further draws attention to the usefulness of EPR measurements at lower frequency to afford access to biologic information deep in living tissues of animals and our dearest among them, the human.

1.2 Tissue Penetration

The most important consideration from the perspective of intended EPR images in human subjects is the ability for the exciting radiofrequency/microwave frequency to reach all parts of a human body. A physicist who understands the primarily non-resonant absorption of electromagnetic energy by lossy living tissue recognizes the importance of reducing the RF frequency to reach deeper into human tissues. We spend a few lines reviewing the physics (Maxwell's equations) of RF penetration of lossy human tissues.

Maxwells equations:

$$\epsilon \nabla \cdot \mathbf{E} = \rho \quad (1)$$

$$\nabla \cdot \mathbf{B} = 0 \quad (2)$$

$$\nabla \times \mathbf{E} + \frac{\partial \mathbf{B}}{\partial t} = 0 \quad (3)$$

$$\frac{1}{\mu} \nabla \times \mathbf{B} - \epsilon \frac{\partial \mathbf{E}}{\partial t} = \mathbf{J} = \sigma \mathbf{E} \quad (4)$$

where ρ is charge density, \mathbf{J} is current density, σ is the material conductivity, \mathbf{E} is the temporally and spatially oscillating electric field intensity with angular frequency ω ($=2\pi \times$ the frequency ν and wavenumber k (2π times the inverse of the wavelength λ), \mathbf{B} is the corresponding magnetic field induction ϵ is the local material

permittivity and μ is the local material permeability. The permittivity can develop an imaginary component when there are dielectric losses as the electromagnetic wave passes through a lossy medium, where the electromagnetic wave causes dipolar molecules to rotate creating frictional losses. Combining these and recalling that the curl of a vector field is the gradient of the divergence minus the Laplacian lead to a wave equation in both E and B

$$\nabla^2 \mathbf{E} - \mu \frac{\partial^2 \mathbf{E}}{\partial t^2} = \sigma \mu \frac{\partial \mathbf{E}}{\partial t} + \nabla \left(\frac{\rho}{\epsilon} \right) \quad (5a)$$

$$\nabla^2 \mathbf{B} - \epsilon \mu \frac{\partial^2 \mathbf{B}}{\partial t^2} = \sigma \mu \frac{\partial \mathbf{B}}{\partial t} \quad (5b)$$

In conducting media, local space charge gradients are rapidly quenched leading to the disappearance of the second term on the left of (5a), the only inhomogeneity in Eqs. (5a, 5b), although this is also a consequence of the general disappearance of longitudinal components of propagating plane waves. (Corson and Lorraine, *Electromagnetic Fields and Waves*, W. H. Freeman, 1962). The result is an attenuated wave equation in the matter for the field vectors \mathbf{E} and \mathbf{B} .

$$\nabla^2 \mathbf{E} - \epsilon \mu \frac{\partial^2 \mathbf{E}}{\partial t^2} = \nabla^2 \mathbf{E} - [1/c_m^2] \frac{\partial^2 \mathbf{E}}{\partial t^2} = \sigma \mu \frac{\partial \mathbf{E}}{\partial t} \quad (6a)$$

where $c_m = 1/\sqrt{\epsilon\mu}$ is the wave speed in medium m and c is the speed in free space.

$$\nabla^2 \mathbf{B} - \epsilon \mu \frac{\partial^2 \mathbf{B}}{\partial t^2} = \nabla^2 \mathbf{B} - [1/c_m^2] \frac{\partial^2 \mathbf{B}}{\partial t^2} = \sigma \mu \frac{\partial \mathbf{B}}{\partial t} \quad (6b)$$

The terms on the left of Eqs. (6a, 6b) are separate second derivatives with respect to space and time allowing a solution that is, if the medium conductivity σ is zero, able to propagate undiminished through space. If the constants for the derivative on the right side of the equation are positive, these are damping terms whose solution is easily characterized by a wave that diminishes in amplitude as it propagates through space depending on σ .

Without too much loss of generality, we can consider the electromagnetic disturbance, \mathbf{E} and \mathbf{B} , to be a planar wave propagating in the z -direction \mathbf{k} . In that case, we can rewrite Eq. (1) as

$$\epsilon \nabla \cdot \mathbf{E} = \epsilon \frac{dE_z}{dz} = \rho \quad (7)$$

and take its second derivative

$$\frac{d^2 E_z}{dz^2} \mathbf{k} = \frac{d(\rho/e)}{dz} \mathbf{k} \quad (8)$$

From Eq. (6a), we have

$$\nabla^2 \mathbf{E} = \frac{d^2 E_x}{dz^2} \mathbf{i} + \frac{d^2 E_y}{dz^2} \mathbf{j} + \frac{d^2 E_z}{dz^2} \mathbf{k} = \epsilon \mu \frac{\partial^2 (E_x \mathbf{i} + E_y \mathbf{j} + E_z \mathbf{k})}{\partial t^2} + \mu \sigma \frac{\partial (E_x \mathbf{i} + E_y \mathbf{j} + E_z \mathbf{k})}{\partial t} + \frac{d(\rho/\epsilon)}{dz} \mathbf{k}.$$

Cancelling the last two terms on each side of Eq. (8) for plane waves $E_{\perp} = E_x \mathbf{i} + E_y \mathbf{j}$ with constant magnitude, just beyond the interface between vacuum ($\epsilon = \epsilon_0, \mu = \mu_0$), and a conducting medium conductivity σ and permittivity ϵ ,

$$\epsilon \frac{\partial^2 E_{\perp}}{\partial t^2} + \sigma \frac{dE_{\perp}}{dt} = 0$$

The frequency of the electromagnetic wave is $\nu = \omega/2\pi$, the angular frequency, then we can write

$$E_{\perp} = E_{\perp 0} e^{-i(kz - \omega t) - z/\delta}$$

where $k = \left(\frac{2\pi}{\lambda}\right) = \frac{\omega}{c_m}$.

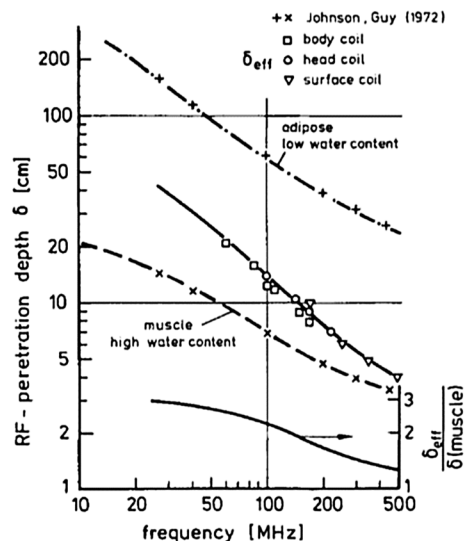
δ is the skin depth, the depth at which E_{\perp} diminishes by $1/e$.

$$\delta = \frac{1}{\left\{ 2\pi\nu \left[\left(\frac{\epsilon\mu}{2}\right)^{\frac{1}{2}} \right] \left[\left(1 + \left(\frac{2\sigma}{\epsilon\nu}\right)^2\right)^{\frac{1}{2}} - 1 \right]^{\frac{1}{2}} \right\}} \sim \sqrt{2/(\pi\nu\sigma\mu)}$$

for a good conductor where $2\sigma/\epsilon\nu \gg 1$.

Figure 1 from Roschmann [4] shows measurements of the effective skin depth from measurements in patients as a function of the radiofrequency roughly verifying the predicted increased fall-off with frequency. A key point is that low RF frequency, significantly less than 1 GHz is necessary to penetrate to the depths of living tissue in the human body. A wealth of information establishes that at $\sim 0.5\text{--}1$ GHz, the absorption of RF energy transitions from dipolar energy interaction with water

Fig. 1 Radiofrequency penetration depth as a function of frequency [4]



to conductive loss through stimulation of conductive oscillations from the dissolved electrolytes in living tissue [5–7]. Perhaps more important is that tomographic reconstruction requires low-frequency electron spin excitation. Deep penetration of tissues for human use will be limited to below 250–300 MHz, corresponding to anatomic imagers using 6.25–7 T magnetic fields for water proton-based MRI. There are at present human systems up to 10.5 T (450 MHz), but these are principally limited to head MRI [8–11].

1.3 Signal-to-Noise at Lower Frequencies in Lossy Living Samples

Simple considerations of the dependence of the signal as a function of frequency would argue that it increases as the square of the frequency ν^2 , one for the increase in the energy levels with the resonant magnetic field and another for the inductive coupling to the resonator. However, similar simple arguments indicate that noise increases as $\nu^{1/2}$ so that SNR increases as $\nu^{3/2}$. Halpern et al. [12] reviewing signal loss in tissues (e.g., Houtl and Lauterbur [13] who concluded with sample losses an SNR frequency dependence of $\sim \nu$) including sample losses opined a much lower loss, $\nu^{0.8}$. This agreed with the subsequent careful analysis by Rinard et al. [14]. Thus, in the context of living samples, oversimplified analysis overestimated the loss in SNR at lower frequencies. There was a good chance that valuable information might be available from images obtained at these frequencies.

1.4 EPR Imaging

1.4.1 The Possibility of EPR-Based Molecular Oxygen Imaging

The absence of molecular oxygen, O_2 , in malignant tissue enhances therapeutic resistance.

Schwarz in 1909 first demonstrated (on himself) the surprising reduced effect of radium γ -ray toxicity in the skin whose blood vessels were occluded [15]. It was soon recognized that virtually all living things were susceptible to hypoxic resistance to radiation. When Thomlinson and Gray [16] found viable tumor layers in sections of lung cancer with remarkably consistent 150-micron thickness, they hypothesized that these represented the diameter of the diffusion cylinder about a tumor feeding capillary, the so-called Krogh cylinder, through which oxygen could pass before being exhausted by cell/tissue metabolism. The edges of these cylinder boundaries clearly demarcated the edge of dead or necrotic lung tissue. They also hypothesized that the edges of the layers would be hypoxic. This hypoxic tissue, “hypoxic rims” would then be the principal source of resistance of malignancy to cancer therapy.

The recognition of the presence of hypoxic resistance ignited a considerable effort in the 1970s to eliminate hypoxia in tumors. An initial set of 100% inhaled oxygen trials failed to show increased tumor control, but emphasized the buffering capability of living systems to regulate relatively narrow limits on viable tissue pO_2 [17]. Trials of three atmospheric pressure 100% hyperbaric oxygen in a 2-in.

thick Plexiglas chamber during radiation treatment compared with normal radiation showed statistically improved local control and survival [18, 19]. However, the complexity of such treatments and the death of an oncologist from an explosion discouraged general acceptance. In the 1980s and 1990, nitroimidazole oxygen mimetic compounds that distribute with more facility in the chaotic vasculature of malignancy than molecular oxygen delivered by hemoglobin in vascular red cells. These again showed promise but provided less advantage and more toxicity than what is necessary to convince clinicians of utility [20].

However, in the 1990s, data were accumulated from multi-sample (typically > 30) local (300 μm diameter volume of sensitivity) polarographic oxygen electrode in multiple types of human tumors. These indicated that (1) tumors have different fractions of tumor hypoxia, defined as a fraction of measurements of $\text{pO}_2 \leq 10$ torr, and (2) tumor control with radiation was statistically significantly double the rate when the mean or median pO_2 was < 10 torr [21]. The question then raised is whether there are tumor regions large enough to identify with the resolution of an EPR-based pO_2 image and whether the direction of radiation based on the EPR pO_2 image can improve tumor control.

1.5 Minimizing Confounding Variables Affecting the Accuracy of EPR pO_2 Oximetry, a Summary

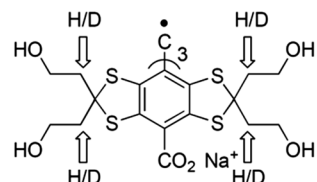
The attraction of using linewidth to measure the dissolved rapidly relaxing paramagnet in a biologic solution is its simplicity. This can be accomplished naturally with continuous wave (CW) techniques or with the theoretically, but not technically equivalent Fourier transform of a free induction decay (FID) using pulse techniques. These techniques allow the recovery of the array of spectral parameters that reflect the environment and motion of the spin probe/spin label, hereafter referred to as the spin probe. However, to focus on the environmental condition of the local O_2 concentration or partial pressure requires desensitization to those effects.

These confounding effects might include temperature dependence of the widths or relaxation rates, but in vivo, this is tightly regulated. Animal environments also rigorously maintain tight constraints on solution tonicity, maintaining them at 310 mOsm. Local viscosity can affect relaxation mechanisms as well, but the development of spin with defined but relevant fluid compartment distribution protects against confounding variation. Labile diffusible metal ions are very difficult to detect in the living system but estimates from scientists and physicians specializing in metal (iron, copper) overload disease opine very low concentration of diffusible paramagnetic metal species. They are rapidly bound by carrying proteins. Hydroxylated metal concentration in aqueous is estimated to have concentrations estimated in the few nanomolar range in the environment [22]. The single major confounding variation from spin probe-based solution measurement of O_2 concentrations or partial pressure is the broadening effect of the spin probe itself, particularly as the O_2 concentration is significantly exceeded by that of the local spin probe, even if the exchange efficiency with the probe is significantly less than that of O_2 [23].

One solution to this has been the development of carbon particulate probes which are, at this writing, either crystals of lithium phthalocyanine [24] or butoxy lithium naphthocyanine [25], or selected carbon chars including specific India inks, the latter of which are the material of human tattoos and, therefore, automatically allowed in human subjects. These materials appear to consist in part of stacks of planar carbon molecules arranged about a pore large enough to freely admit O_2 molecules. These materials have a high unpaired electron density which rapidly exchanges along the pore surface. Di-paramagnetic molecular oxygen interferes with the rapid exchange, increasing the width of the exchange narrowed Lorentzian EPR signal. This gives these species high signal and high change in linewidth as a function of pO_2 . They are most often prepared as a slurry of material and injected into animal tissue or, in the case of India inks, the skin or several mm linear dimension of tissue and detected from the animal surface using surface coils. Batches of the phthalocyanine crystals and other carbon chars have a sample-dependent linewidth vs pO_2 calibrations requiring individual sample calibration, likely due to the heterogeneity of crystal morphology. Particulates have been used in single or multisite spectroscopic oximetry but not in animal imaging. What is particularly attractive about these molecules is that the oximetry takes place in the internal pore of the crystals and, therefore, not susceptible to effects external to the crystal pore. This substantially frees the measurements from the above confounding variation. Repeatable measurements have been performed using India ink in human subjects over periods of years [26].

The second approach has involved fortuitous spin probes and pulse spin–lattice relaxation techniques enabled by these spin probes. As noted above, there is a variety of infusible soluble spin probes, which can be chosen according to their octanol partition coefficients to distribute variably but controllably in various tissue compartments: intravascular, interstitial but extravascular and extracellular, and intracellular. Nitroxides have been extensively reviewed [27]. A remarkable group of tri-acid carbon-centered spin probes, MW 1.1–1.8 KD was developed by Lars-Goren Svensen, Jan Henrik Ardenkjaer-Larsen, and Klaes Golman in the Nycomed subsidiary of what is now GE Healthcare [28]. The size and triple anionic character of the molecules limited them to extracellular distribution. The alcoholic decorations on the sulfur bridging carbons of this tri-aryl molecule shown in Fig. 2 minimized toxicity to the point where rodent models tolerated hours of infusion on multiple occasions with extremely low noted toxicity attributable to the spin probe. The deuterated form referred to as OX071 Fig. 2 has an 8 μ T hypoxic linewidth and a strong signal at local animal tumor concentrations of 200–300 μ M. The OX071 hypoxic longitudinal relaxation time T_1 is 7 μ s and

Fig. 2 OX071 with deuteration site indicated



its transverse relaxation time T_2 is 6 μs contrasting with nitroxides whose longest hypoxic T_1 is 1 μs and T_2 is 0.5 μs at 250 MHz. This near order of magnitude increase in relaxation time enables pulse acquisition.

1.6 Evolution of our Approach to pO_2 Imaging in the Tumors of Live Mammals

Our initial approach to quantitative oximetry and oximetric imaging was to use a four-dimensional spectral-spatial imaging technique with signal overmodulation [29], and fixed-stepped gradient direction and amplitude tomographic image acquisition over periods from 30 to 45 min [29, 30]. Beginning in 2006, we started to use stepped gradient direction tomographic image acquisition with electron spin echo (ESE) and phase relaxation images [31]. During the period from 2008 to 2010, with careful maintenance of the signal amplitude during image acquisition, we obtained oxygen images in animal tumors with hypoxic voxel pO_2 resolution of 5–7 torr [32]. In 2010, we realized that spin–lattice relaxation (SLR) inversion recovery images with a fixed echo electron spin echo readout (IRESE) improved the hypoxic voxel resolution for our normal 10-min images to 1 torr as shown in Fig. 3 [33, 34].

The reason behind this is that spin–lattice relaxation pathway is associated with the spin probe magnetization energy deposition into the two unpaired spins of

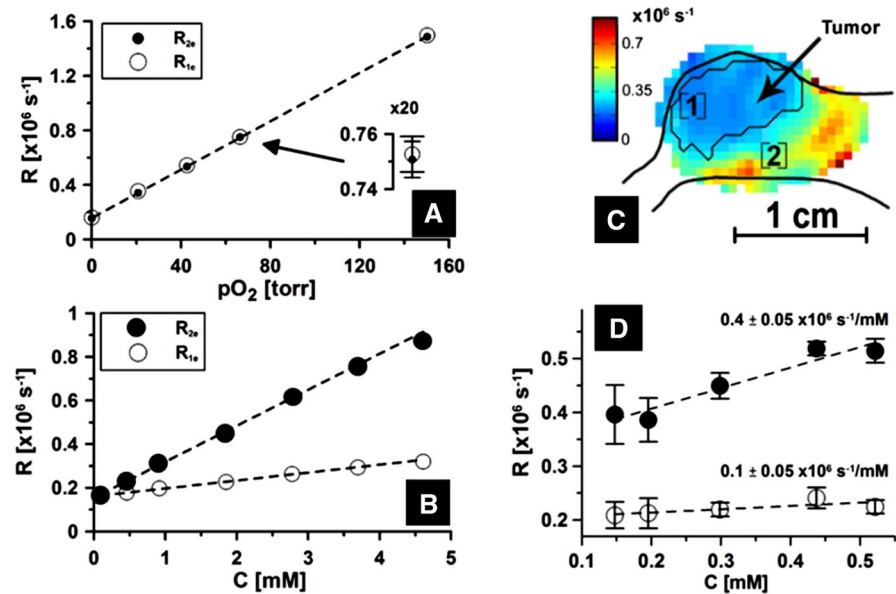


Fig. 3 **a** Comparison of SLR relaxation homogeneous sample measurements $R_{1e}=1/T_{1e}$ response to pO_2 (open circle) with that of ESE relaxation $R_{2e}=1/T_{2e}$ (filled circle) (note shift of R_{2e} intercept). **b** Comparison of R_{1e} (open circle) response to spin probe concentration with that of R_{2e} (filled circle). Slope of R_{2e} is 4.86 that of R_{1e} . **c** Sagittal plane from leg tumor pO_2 image with tumor [52] and normal tissue [53] region indicated. **d** Comparison of in vivo response of R_{1e} (filled circle) with that of R_{2e} to spin probe concentration. Slope ratio is similar to that of **B** [33, 34]

oxygen, while phase relaxation can be sensitive to spin–spin interaction and associated relaxation pathways that bear strong dependence on spin probe concentrations and other environmental parameters. The upper bounds on concentrations of other diffusible paramagnetic species are several orders of magnitude smaller than those of oxygen and the spin probe. Beginning in 2010, IRESE has been used to obtain pO_2 images.

1.7 Can EPR pO_2 Imaging at Low Frequencies Provide Compelling Evidence for Advantage Hypoxia Targeting with Radiation

In addition to his pioneering work in high-field EPR, Yacov Lebedev pioneered in the development of EPR imaging [3]. Our interest in imaging has, since its inception, been stimulated by the early publication of Backer et al. [35] demonstrating the sensitivity of the superhyperfine spectral definition of a nitroxide spin label/spin probe to the solution concentration of molecular oxygen. This, in turn, was based on the Freed group publication of Heisenberg spin exchange as a principal mechanism by which dissolved paramagnetic materials broadened spectral line, a spin–spin exchange mechanism [36, 37]. The appreciation of the possibility of a quantitative molecular oxygen image based on spectroscopic [38] or spectral-spatial [39, 40] EPR image was stimulated by these convergent developments.

The construction of a 250 MHz imaging spectrometer capable in principle of distinction of two adjustable orthogonal horizontal magnetic field gradients to produce a two-dimensional spatial-one-dimensional spectral image [41] furthered this possibility.

1.8 Imaging Technique

CW image methods: each gradient was generated by two pairs of rectangular current loops. Each pair generated a relatively uniform magnetic field but in opposite directions creating a linear gradient field between them. Each quadruple of coils was powered by one axis of a Copley 262 switching mode gradient supply. The gradient parallel to the main field was a Maxwell pair. The main field was a four-coil 8th-order corrected coil set as described by Rinard [42]. The gradient magnetic fields generate 66 spatial directions and 14 spectral angles, i.e., gradient magnitudes maximum 30 mT/m, overall 924 projections with a spatial field of view 3.0 cm and a spectral field of view of 0.1 mT. Imaging time was 30 min. Simple 1 loop–1 gap loop gap resonators were used [31].

Pulse image methods: the above gradients and main magnet were used. Equal solid spatial angle gradient scheme used 208 projections; gradient magnitude = 15 mT/m; field of view 4.24 cm; baseline acquired every fourth trace overall 53 traces; 35 ns $\pi/2$ and π RF pulses, 16-step phase cycling, 40,000 acquisitions, including phase cycling; images with five different τ for ESE [31] or eight different T_s for IRESE [33, 34] logarithmically spaced.

1.9 The Biologic Validation of EPR pO_2 Imaging

We briefly review a few validating experiments from the three different pO_2 imaging approaches from our laboratory.

1.10 Can EPR pO_2 Images Obtained With CW Spectral-Spatial Images Correlate Point by Point With Oxylite Phosphorescence Quenching pO_2 Measurements?

Oxylite is the successor to the Eppendorf needle electrode referred to above as re-establishing the appreciation of the correlation between tumor failure when treated with radiation therapy and the fraction of tumor samples with pO_2 less than a specific threshold, most commonly 10 torr. We developed a stereotactic needle holder shown in Fig. 4 from which to launch the Oxylite fiberoptic probe into a tumor while the tumor was located and immobilized in the imager resonator. Without significant perturbation of the tumor immobilized in a rubbery semi-circumferential dental mold, cast (Ennimax, vinyl polysiloxane) was punctured with a sharp scalpel and the 230 μm diameter optical (glass) fiber was pushed into the tumor tissue to the opposite side of the tumor and then withdrawn in 1 mm steps. An equilibration time of 1 min was taken before recording the relaxation signals from a 250–300 diameter Ruthenium-III-(Tris)chloride embedded in silicone polymer excited by a pulse from the blue light-emitting diode [43].

In Fig. 5, two orthogonal pO_2 slices of the pO_2 image are shown. They intersect at the path of the Oxylite track shown as the black line in Fig. 5a, c. Quantitative pO_2 values from both the Oxylite track and two adjacent pO_2 image tracks are shown in Fig. 5b. Coordinates refer to the image coordinates with zero offset approximately in the center of the resonator and the tumor. Figure 5a shows a sagittal slice of the quantitative tumor oxygenation image with a color

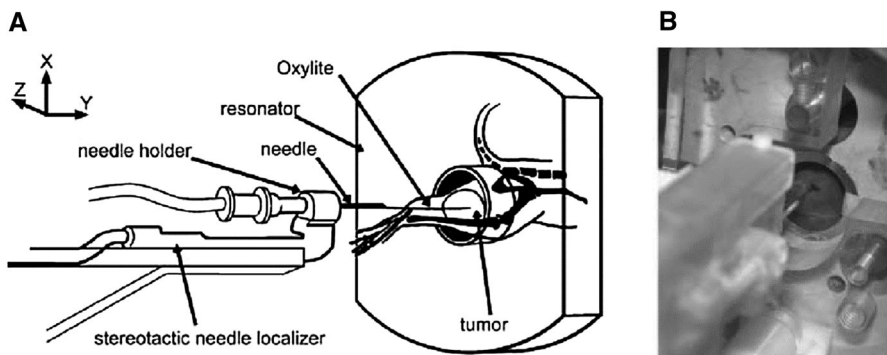


Fig. 4 Diagram and photograph of the Oxylite probe, mounted in the stereotactic frame and penetrating the FSa tumor in the hind leg of a C3H mouse immobilized in the EPR resonator. The Oxylite probe was advanced to the length of the tumor. Spatial coordinates of probe tip can be controlled within 2-mm accuracy. For scale, the diameter of the tumor-bearing inductive element of the resonator (the hole through which the tumor-bearing leg extends) is 16 mm. **a** Diagram of the stereotactic mount for the delivery of the Oxylite probe. **b** Photograph of the same showing the Oxylite probe penetrating the tumor

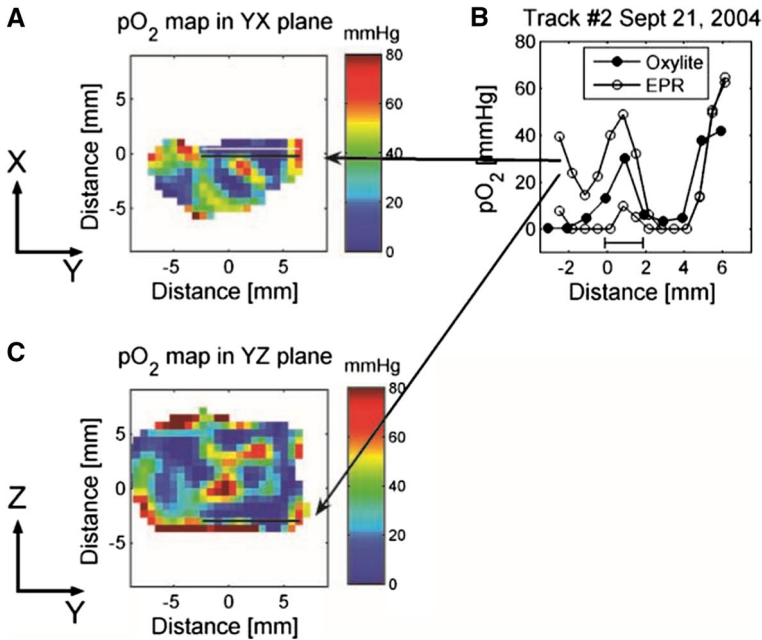


Fig. 5 a, c EPR Orthogonal pO_2 image planes through the Oxylite tracks. **b** (Open circle) pO_2 values from adjacent tracks in image c (filled circle) Oxylite pO_2 values [43]

bar representing the fitted Lorentzian spectral width-based pO_2 estimate of each image voxel. This is derived from the four-dimensional EPR pO_2 spectral-spatial image of the tumor-bearing leg, the example of which is shown in Fig. 4. In c, adjacent tracks are shown in black and white in the coronal image. The Oxylite track values (filled circle) and the two adjacent black and white tracks' pO_2 values from (c) (open circle) are shown in Fig. 5b. The oxygen image "track" with the higher values corresponds to the black track in Fig. 5c. The error bar along the abscissa of Fig. 5b represents needle location uncertainty (2 mm). The disagreement between image and Oxylite at the right of Fig. 5b is expected since this is the entrance of the needle where the scalpel has disrupted the tissue. Another sixteen tracks with similar agreements are shown in Elas et al. [43].

Do multi-voxel pO_2 sample hypoxic fractions defined by CW spectral-spatial images significantly correlate with tumor sample hypoxia proteins?

A striking and perhaps expected finding of the 1990s was the existence of an array of correlated cell, tissue, organ, and organism molecular biology pathways responsive to local hypoxia. For the discovery of Hypoxia Inducible Factor(s), HIF, [44, 45] Gregg Semenza was awarded part of the 2019 Nobel Prize in Physiology or Medicine. A test of the physiologic relevance of pO_2 images lies in its ability to correlate with hypoxia response proteins known to be increased in response to hypoxia. Vascular endothelial growth factor, VEGF was among the original proteins involved in the molecular response to hypoxia to increase

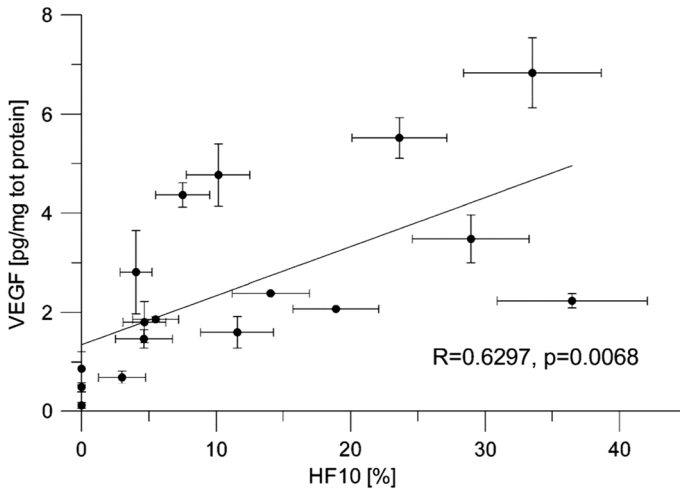


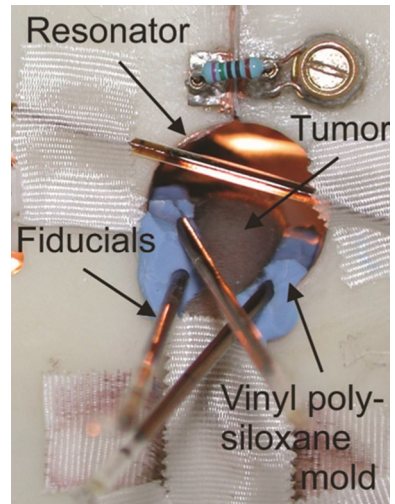
Fig. 6 Sample VEGF concentration plotted against sample hypoxic fraction (voxel fraction ≤ 10 torr). Pearson correlation coefficient R assuming linear relationship, fraction of effect on protein concentration due to change in. p is significance of the variation [47]

micro-vessel proliferation of putatively hypoxic regions of tumors [46]. Using the same stereotactic platform described above with the fiberoptic probe replaced by an 11 gauge bone biopsy needle, cores of tumor tissue were obtained each containing two or three 200–300 voxel (60–90 μl) samples. These were sufficient to evaluate the 10 torr or below a hypoxic fraction of voxels in each sample and obtain the concentration of VEGF evaluated with an enzyme-linked immunosorbent assay (ELISA) for each sample. A significant correlation is shown in Fig. 6 [47].

1.11 Can a Combination of CW Spectral-Spatial EPR $p\text{O}_2$ Images and Pulse Electron Spin Echo Images Define Resistant and Sensitive Tumors as Did the Eppendorf Polarographic Needle Electrode?

A critical requirement to determine the true hypoxic fraction in a tumor is precise definition of the tumor boundaries. Given how the Eppendorf electrode $p\text{O}_2$ readings were obtained from a tumor [21], this was not thought to be crucial. However, radiation oncologists have come to agree in many, if not all malignancies that true tumor contrast is provided by T2-weighted MRI. Tumor contrast was recognized in the inception of MRI [48–50]. It continues to be used to stage tumors of the uterine cervix among other tumor types [51]. This requires the techniques to immobilize tumors so that images will be obtained with the tumor-bearing anatomy in the same position for multiple image acquisition. Fiducials, simple geometric objects (sealed tubes with contrast materials visible in all images) must be placed in the image field. This allows registration of the various image data for proper colocalization of the different information in each of the images. Figure 7 shows an example of the semi-circumferential vinyl polysiloxane mold that minimizes compression of a leg-born

Fig. 7 Mouse leg with FSa tumor in the resonator [52]



tumor that will fit into various cylinders in the image acquisition instruments and fiducials to register image datasets [52].

Two separate tumor types FSa fibrosarcomas and MCA4 mammary adenocarcinomas were grown in the gastrocnemius muscle in the legs of C3H mice to volumes of $450 \pm 100 \mu\text{l}$. The tumors were imaged with both T2-weighted MRI and CW EPR $p\text{O}_2$ imaging. The MRI provided a three-dimensional tumor margin image allowing the assessment of the number of $p\text{O}_2$ image voxels with $p\text{O}_2$ values ≤ 10 torr within the tumor margin. This in turn allows the assessment of the tumor hypoxic fraction.

The FSa sarcomas were treated with a Phillips RT 250 orthovoltage X-ray machine to a radiation dose obtained in separate experiments to cure 50% of tumors the 50% tumor control dose or $\text{TCD}_{50} = 33.8$ Gy. The MCA4 adenocarcinomas were treated to a range of doses about the $\text{TCD}_{50} = 69$ Gy. The FSa sarcomas were followed for 90 days, while the MCA4 adenocarcinomas were followed for 120 days, the intervals found to allow the recurrence of each tumor type. This treatment paradigm is referred to as a clonogenic assay, determining the dose of a toxin necessary to prevent the last tumor cell from proliferating and regrowing to a tumor. The data are presented in Fig. 8 [52]. The difference between large and small hypoxic fraction tumors is statistically significant for all data presented. The control of FSa fibrosarcomas were treated with a 50% control dose (TCD_{50}) of radiation, the fraction of whose voxels with $p\text{O}_2 < 10$ torr that was $< 10\%$ of those of the whole tumor compared with those with a $\text{HF}_{10} > 10\%$ differed with $p = 0.0138$. For the MCA4 tumors treated with a 20 Gy range of doses distributed about the 69 Gy TCD_{50} with $\text{HF}_{10} < 10\%$ compared with $\text{HF}_{10} > 10\%$ tumors, the comparison using K–M analysis showed a $p = 0.0072$ likelihood that the populations are the same. Using a slightly higher hypoxic fraction and a smaller dose range, the same comparison showed $p = 0.0193$.

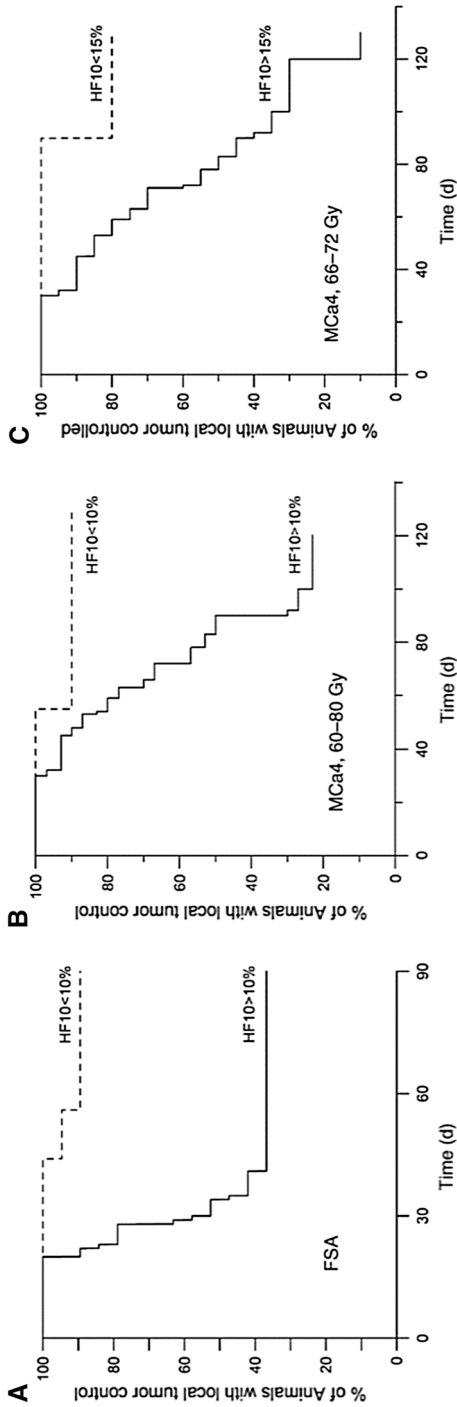


Fig. 8 **a** Kaplan–Meier (KM) survival plot comparing the control of FSA tumors all treated with 33.8 Gy radiation for whom > 10% of tumor voxels had $pO_2 < 10$ torr (HF10 < 10 torr) with those whose HF10 was > 10%. **b** Kaplan–Meier (KM) survival plot comparing the control of MCa4 tumors treated with a range of doses about the TCDS50 of 69 Gy radiation for whom > 10% of tumor voxels had $pO_2 < 10$ torr (HF10 < 10 torr) with those whose HF10 was > 10%. **c** Kaplan–Meier (KM) survival plot comparing the control of FSA tumors for whom > 15% of tumor voxels had $pO_2 < 10$ torr (HF10 < 10 torr) with those whose HF10 was > 10% [52]

Both of the measurement techniques required very careful attention paid to the infusion rate of the spin probe since there was a concentration/signal amplitude dependence of the apparent pO_2 values giving a 5–7 torr uncertainty in the pO_2 values near zero and larger uncertainties at higher values. Nonetheless, the EPR pO_2 images clearly defined the effect of pO_2 as measured with EPR on tumor control. This argues that should EPR technology, including the spin probe, be approved for human use, it might provide an image to define more radiation-resistant tumors.

1.12 Can EPR pO_2 Images Beneficially Direct Radiation to Resistant Portions of a Tumor, Potentially Enhancing Therapeutic Efficacy?

For the images in this study, the IRESE spin lattice relaxation rate images shown in Fig. 3 were used exclusively [53].

The general benefit provided by preclinical EPR pO_2 images is the resolution of the controversy about the clinical relevance of tumor hypoxia. These images can determine if the hypoxic resistant tumor portions can be localized and selectively treated with extra radiation, referred to as boost doses. Present radiation therapy technology uses multi-leaf collimators that dynamically adjust the aperture through which the radiation is delivered to patient tumors. This allows radiation dose plans to provide steep spatial gradients in dose to avoid critical structures with specific dose thresholds beyond which life-altering complications will have increased probability. From the 124-year history of radiation delivery, it has also been observed that such gradients within the tumor volume also produce these complications. One of the Radiation Therapy Oncology Group (RTOG) radiation plan limits is the amount of variation within the tumor volume. There has not been the convincing demonstration that there are regions within human tumors that could beneficially be targeted with a radiation dose “hot spot”.

There are several limitations in demonstrating this in preclinical animal tumor models whose tumors have been extensively studied over the past 60 years of preclinical research. The most cost-effective and best studied animal is the mouse. Its volume is 3000 times smaller than that of the average 70 kg male human, although this reduces the linear dimension scale by a factor of 15 roughly scaling cm to mm. Multi-leaf collimators have been tried with leaf thickness reduced to millimeters but have not been widely used. Technologies utilizing a scanning pencil radiation beam are another alternatives but may be time-consuming and cumbersome.

Radiation delivery has been found optimal using an isocentric machine, where the radiation source rotates on a fixed gantry about the immobilized patient on a table whose position is repeatable to within 1 mm. The recent development of the XRAD225Cx radiator and CT machine (Fig. 9a) for mouse and rat radiation has fulfilled part of this need (Supplementary Materials).

The second technical achievement has been the development of radiation block printing. This technique was used for much larger clinical systems, where 3D-printed plastic blocks loaded with tungsten provided apertures that conform to the margins of complex tumors. It was not unreasonable to consider such printed blocks to be inserted in the head of the XRAD mouse radiator to deliver radiation

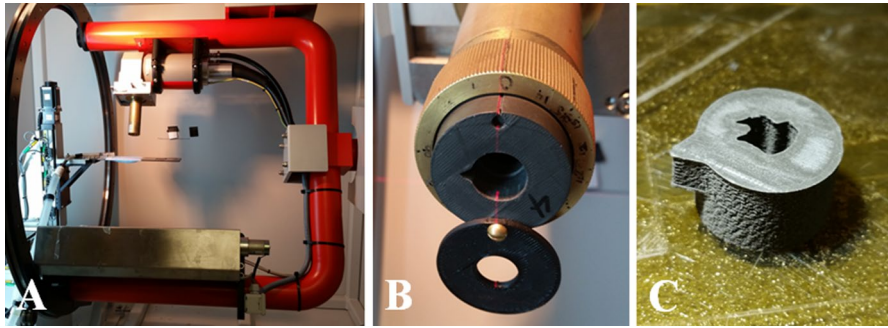
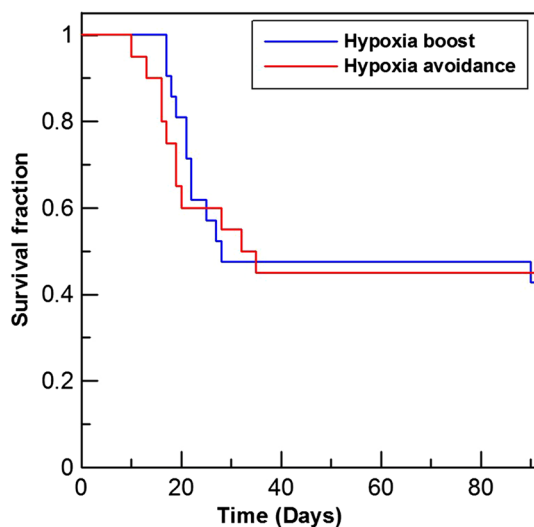


Fig. 9 XRAD225Cx CT imager and irradiation system. **b** Collimator with 3D-printed radiation block holder with key to the left to orient the block. **c** 3D-printed tungsten loaded plastic radiation block (Supplementary Materials)

boosts to hypoxic resistant portions of the tumor and avoid well-oxygenated more sensitive tumor regions. Examples of such a block are shown in Fig. 9b, c (Supplementary Materials).

In the experiments to be described, a prior set of experiments were performed to determine the tumor control vs whole tumor dose, the TCD finding experiments. Because of the extensive hypoxia in $450 \pm 100 \mu\text{l}$ tumors in the prior experiments, $350 \pm 100 \mu\text{l}$ volumes were used for FSa sarcoma study. Initial experiments attempted to demonstrate the advantage of tumor boosts using simple spherical radiation volumes covering $\sim 85\%$ of hypoxia and compared these crude hypoxia boost with boosts to shells of rotation to the usually peripheral well-oxygenated tumor regions. All of the tumors were treated to a 30% control dose and a 5 Gy boost (the additional whole tumor dose necessary to control 90% of tumors) was given to either hypoxic or well-oxygenated regions. The depressing lack of benefit shown in

Fig. 10 Kaplan–Meier analysis comparing incomplete hypoxic boost with hypoxia avoidance boost of similar volume. All of the tumors were treated to a 30% control dose and 5 Gy (the additional whole tumor dose necessary to control 90% of tumors) was given to either hypoxic or well-oxygenated regions (Supplementary Materials)



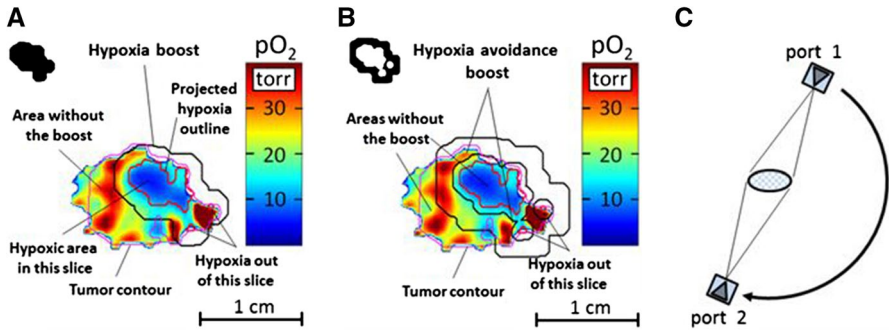
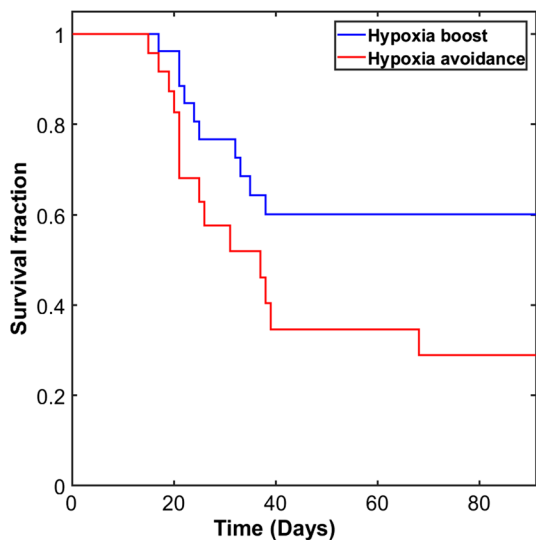


Fig. 11 Radiation treatment plans and delivery scheme. **a.** EPR pO_2 image slice orthogonal to the radiation beam showing hypoxia boost treatment plan. **b.** The same EPR pO_2 image slice showing hypoxia avoidance boost. Magenta contour: MRI-defined tumor margin. Red contour: projection of all in-tumor hypoxic volumes onto the EPR image plane. Black contours—radiation treatment beam shape including additional setup uncertainty margins. The area of the hypoxia avoiding boost equals the area of the hypoxia boost. Note in both **a** and **b** the islands of hypoxia out of the plane derived from the DRR of the whole tumor volume as well as the margin about the hypoxia, 1.2 mm for the hypoxia boost and 0.6 mm for the hypoxia avoiding boost. Upper left corners of **a** and **b**: black shapes of hypoxic boost (**a**) and well-oxygenated boost (**b**) apertures. **c** Illustration of opposed field radiation boost treatment with XRAD225Cx gantry-mounted X-ray machine. Each field was treated with half of the total boost dose [53]

Fig. 10 ($p=0.98$) convinced us of the need to target far more than 85% of the resistant hypoxia; > 98% of hypoxic voxels needed to be covered for the hypoxic boost (Supplementary Material, ref. 53).

For simplicity in using treatments that distinguish boost treatment to the hypoxic tumor from boosts to well-oxygenated tumor, opposed oblique fields were chosen for the boosts (Fig. 11c). A 15% control dose for FSa tumors was first administered

Fig. 12 Kaplan–Meier survival plot comparing conformal hypoxia boost with hypoxia avoidance boost. The outcome from the two treatments show control populations that differ significantly ($p=0.04$) demonstrating the therapeutic efficacy of hypoxia guided radiation [53]



to each tumor. MRI outlined the tumor and EPR pO_2 images defined all hypoxic voxels including single disconnected hypoxic voxels. The contours of the tumor and hypoxic voxels were collapsed onto an image of the central plane of the tumor-bearing C3H mouse leg (Fig. 11a, b). The hypoxic tumor boost is shown in Fig. 11a. The well-oxygenated tumor boost is shown in Fig. 11b. Figure 12 shows the strategy for the treatment of the FSa fibrosarcomas randomized treatment. Kaplan–Meier analysis of the outcomes of boost treatments randomly assigned to the hypoxic tumor or well-oxygenated tumor is shown for the FSa fibrosarcomas in Fig. 12.

As noted above, hypoxic resistance to radiation has been known for nearly a one-and-a-quarter century. Attempts to overcome this to enhance cancer therapy have stimulated enormous effort to apply simple solutions to an extraordinarily complicated system as has been defined by Gregg Semenza and an international group of colleagues. One other relatively simple addition to the manifold enhancements of this therapy would be to define resistant regions of the proper size to make it amenable to radiation boosts in human subjects. Until the data presented in Fig. 12 were published [53], there have been no data published to identify and then beneficially treat resistant hypoxic tumor regions in mammalian tumors. As noted, this appears to be true in a second mammalian tumor system (unpublished data).

2 Conclusion

EPR pO_2 measurements in animal systems managed to circumvent numerous technical challenges associated with SNR losses and variability of the spin-probe environment affecting the accuracy. The EPR pO_2 images and applications described here involved the development of techniques that provide sufficient resolution to observe medically relevant effects in live subjects and sufficient accuracy to provide significant biological data. In fact, pO_2 images acquired using EPR have become the “gold standard” of non-invasive in vivo and in vitro measurements. They have provided transformative data that promise improvements in therapy delivery to patients, pending much technical progress.

The early imaging studies from Yacov Lebedev’s laboratory were part of the foundation upon which the present imaging research is based. We review it in celebration of all the wonderful work produced under Professor Lebedev’s guidance.

Acknowledgements Funding was provided by National Cancer Institute (Grant no. R01 CA098575 R01 CA236385) and National Institute of Biomedical Imaging and Bioengineering (Grant nos R01EB029948, P41 EB002034).

References

1. E. Zavoisky, *J. Phys.* **9**, 245 (1945)
2. Y.S. Lebedev, *Appl. Magn. Reson.* **7**, 339–362 (1994)
3. E.V. Galtseva, O.Y. Yakimchenko, Y.S. Lebedev, *Chem. Phys. Lett.* **99**, 301–304 (1983)
4. P. Roschmann, *Med. Phys.* **14**, 922–931 (1987)

5. C.C. Johnson, A.W. Guy, *Proceedings of the IEEE* **60**, 692–718 (1972)
6. H.P. Schwan, K.R. Foster, *Proceedings of the IEEE* **68**, 104–113 (1980)
7. J.L. Schepps, K.R. Foster, *Phys. Med. Biol.* **25**, 1149–1159 (1980)
8. J.T. Vaughan, C.J. Snyder, L.J. DelaBarre, P.J. Bolan, J. Tian, L. Bolinger, G. Adriany, P. Andersen, J. Strupp, K. Ugurbil, *Magn. Reson. Med.* **61**, 244–248 (2009)
9. N. Zhang, X.H. Zhu, E. Yacoub, K. Ugurbil, W. Chen, *Exp. Brain Res.* **204**, 515–524 (2010)
10. X.X. He, M.A. Erturk, A. Grant, X.P. Wu, R.L. Lagore, L. DelaBarre, Y. Eryaman, G. Adriany, E.J. Van de Auerbach, P.F. Moortele, K. Ugurbil, G.J. Metzger, *Magn. Reson. Med.* **84**, 289–303 (2020)
11. A. Sadeghi-Tarakameh, L. DelaBarre, R.L. Lagore, A. Torrado-Carvajal, X. Wu, A. Grant, G. Adriany, G.J. Metzger, P.F. Van de Moortele, K. Ugurbil, E. Atalar, Y. Eryaman, *Magn. Reson. Med.* **84**, 484–496 (2020)
12. H.J. Halpern, M.K. Bowman, in *EPR Imaging and in vivo EPR*, ed. by G.R. Eaton, S.S. Eaton, K. Ohno (CRC Press, Boca Raton, 1991) Chapt 6
13. D.I. Hoult, R.E. Richards, *J. Magn. Reson.* **24**, 71–85 (1976)
14. G.A. Rinard, R.W. Quine, S.S. Eaton, G.R. Eaton, in *Biological Magnetic Resonance*, vol. 21, ed. by C. Bender, L.J. Berliner (Kluwer Academic/Plenum Pub. Corp., New York, 2004) pp. 115–154.
15. G. Schwarz, *Munchner Medizinische Wochenschrift* **56**, 1217–1218 (1909)
16. R.H. Thomlinson, L.H. Gray, *Br. J. Radiol.* **9**, 539–563 (1955)
17. M.R. Horsman, A.A. Khalil, M. Nordmark, C. Grau, J. Overgaard, *Radiother. Oncol.* **28**, 69–71 (1993)
18. J.M. Henk, P.B. Kunkler, C.W. Smith, *Lancet* **2**, 101–103 (1977)
19. J.M. Henk, C.W. Smith, *Lancet* **310**, 104–105 (1977)
20. C.N. Coleman, J.B. Mitchell, *J. Clin. Oncol.* **17**, 1–3 (1999)
21. M. Hockel, K. Schlenger, S. Hockel, P. Vaupel, *Cancer Res.* **56**, 4509–4515 (1996)
22. W. Stumm, J.J. Morgan, *Aquatic Chemistry: Chemical Equilibria and Rates in Natural Waters*, 3rd edn. (Wiley, New York, 1995)
23. Y.N. Molin, K.M. Salikhov, K.I. Zamarayev, *Spin Exchange: Principles and Applications in Chemistry and Biology* (Springer, Berlin, 1980)
24. K.J. Liu, P. Gast, M. Moussavi, S.W. Norby, N. Vahidi, T. Walczak, M. Wu, H.M. Swartz, *Proc. Natl. Acad. Sci. USA* **90**, 5438–5442 (1993)
25. G. Ilangovan, A. Manivannan, H. Li, H. Yanagi, J.L. Zweier, P. Kuppusamy, *Free Radic. Biol. Med.* **32**, 139–147 (2002)
26. B.B. Williams, N. Khan, B. Zaki, A. Hartford, M.S. Ernstoff, H.M. Swartz, *Adv. Exp. Med. Biol.* **662**, 149–156 (2010)
27. L.J. Berliner (ed.), *Spin Labels*, vol. 1 (Academic Press, New York, 1976)
28. J.H. Ardenkjaer-Larsen, A.M. Leach, N. Clarke, J. Urbahn, D. Anderson, T.W. Skloss, *J. Magn. Reson.* **133**, 1–12 (1998)
29. C. Mailer, B.H. Robinson, B.B. Williams, H.J. Halpern, *Magn. Reson. Med.* **49**, 1175–1180 (2003)
30. M. Elas, B.B. Williams, A. Parasca, C. Mailer, C.A. Pelizzari, M.A. Lewis, J.N. River, G.S. Karczmar, E.D. Barth, H.J. Halpern, *Magn. Reson. Med.* **49**, 682–691 (2003)
31. B. Epel, S.V. Sundramoorthy, E.D. Barth, C. Mailer, H.J. Halpern, *Med. Phys.* **38**, 2045–2052 (2011)
32. B. Epel, S.V. Sundramoorthy, C. Mailer, H.J. Halpern, *Concept Magn. Reson. B.* **33B**, 163–176 (2008)
33. B. Epel, M.K. Bowman, C. Mailer, H.J. Halpern, *Magn. Reson. Med.* **72**, 362–368 (2014)
34. B. Epel, H.J. Halpern, *J. Magn. Reson.* **254**, 56–61 (2015)
35. J.M. Backer, V.G. Budker, S.I. Eremenko, Y.N. Molin, *Biochim. Biophys. Acta* **460**, 152–156 (1977)
36. P.E. Eastman, R.G. Kooser, M.R. Pas, J.H. Freed, *J. Chem. Phys.* **54**, 2690 (1969)
37. M.P. Eastman, G.V. Bruno, J.H. Freed, *J. Chem. Phys.* **52**, 2511 (1970)
38. P.C. Lauterbur, D.N. Levin, R.B. Marr, *J. Magn. Reson.* **59**, 536–541 (1984)
39. M.M. Maltempo, *J. Magn. Reson.* **69**, 156–161 (1986)
40. M.M. Maltempo, S.S. Eaton, G.R. Eaton, *J. Magn. Reson.* **72**, 449–455 (1987)
41. H.J. Halpern, D.P. Spencer, J. Vanpolen, M.K. Bowman, A.C. Nelson, E.M. Dowey, B.A. Teicher, *Rev. Sci. Instrum.* **60**, 1040–1050 (1989)
42. G.A. Rinard, R.W. Quine, G.R. Eaton, S.S. Eaton, E.D. Barth, C.A. Pelizzari, H.J. Halpern, *Concept Magn. Res.* **15**, 51–58 (2002)

43. M. Elas, K.H. Ahn, A. Parasca, E.D. Barth, D. Lee, C. Haney, H.J. Halpern, *Clin. Cancer Res.* **12**, 4209–4217 (2006)
44. G.L. Semenza, *Cell* **107**, 1–3 (2001)
45. G.L. Semenza, *Cancer Metas. Rev.* **26**, 223–224 (2007)
46. J. Folkman, E. Merler, C. Abernathy, G. Williams, *J. Exp. Med.* **133**, 275–288 (1971)
47. M. Elas, D. Hleihel, E.D. Barth, C.R. Haney, K.H. Ahn, C.A. Pelizzari, B. Epel, R.R. Weichselbaum, H.J. Halpern, *Mol. Imaging Biol.* **13**, 1107–1113 (2011)
48. R. Damadian, *Science* **171**, 1151–1153 (1971)
49. R. Damadian, K. Zaner, D. Hor, T. DiMaio, *Proc. Natl. Acad. Sci. USA* **71**, 1471–1473 (1974)
50. R. Damadian, K. Zaner, D. Hor, T. DiMaio, L. Minkoff, M. Goldsmith, *Ann. NY Acad. Sci.* **222**, 1048–1076 (1973)
51. S. Fridsten, A.C. Hellstrom, K. Hellman, A. Sundin, B. Soderen, L. Blomqvist, *Acta Radiol. Open* **5**, 2058460116679460 (2016)
52. M. Elas, J.M. Magwood, B. Butler, C. Li, R. Wardak, R. DeVries, E.D. Barth, B. Epel, S. Rubinstein, C.A. Pelizzari, R.R. Weichselbaum, H.J. Halpern, *Cancer Res.* **73**, 5328–5335 (2013)
53. B. Epel, M.C. Maggio, E.D. Barth, R.C. Miller, C.A. Pelizzari, M. Krzykawska-Serda, S.V. Sundramoorthy, B. Aydogan, R.R. Weichselbaum, V.M. Tormyshev, H.J. Halpern, *Int. J. Radiat. Oncol. Biol. Phys.* **103**, 977–984 (2019)

Publisher's Note Springer Nature remains neutral with regard to jurisdictional claims in published maps and institutional affiliations.